LA-UR-15-24719 (Accepted Manuscript)

In Situ X-Ray Observations of Dendritic Fragmentation During Directional Solidification of a Sn-Bi Alloy

Gibbs, John W.
Tourret, Damien
Gibbs, Paul J.
Imhoff, Seth D.
Gibbs, Meghan Jane
Walker, Brandon
Fezzaa, Kamel
Clarke, Amy Jean

To be published in: JOM

DOI to publisher's version: 10.1007/s11837-015-1646-7

Permalink to record: http://permalink.lanl.gov/object/view?what=info:lanl-repo/lareport/LA-UR-15-24719

In situ X-ray observations of dendritic fragmentation during directional solidification of a Sn-Bi alloy

John W. Gibbs[1*], Damien Tourret[1], Paul J. Gibbs[1,2], Seth D. Imhoff[1], Meghan J. Gibbs[1], Brandon A. Walker[1], Kamel Fezzaa[3], Amy J. Clarke[1]

[1] Materials Science and Technology Division, Los Alamos National Laboratory
[2] Hydrogen and Materials Science, Sandia National Laboratory
[3] Advanced Photon Source, Argonne National Laboratory
* jwgibbs@lanl.gov

Abstract

Dendrite fragmentation is an important phenomenon in microstructural development during solidification. For instance, it plays a key role in initiating the columnar-to-equiaxed transition. Here, we use X-ray radiography to study dendrite fragmentation rate in a Sn-39.5 wt% Bi alloy during directional solidification. Experiments are performed in which solidification is parallel and anti-parallel to gravity, leading to significantly different fragmentation rates. We quantify the distribution of fragmentation rate as a function of distance from the solidification front, time in the mushy zone, and volume fraction of solid. While the observed fragmentation rate can be high, there is no evidence of a columnar-to-equiaxed transition, illustrating that it requires more than just fragmentation to occur.

Introduction

The fragmentation of dendrites during solidification can have a variety of effects in metal castings. The columnar-to-equiaxed transition (CET), for instance, has been attributed to fragments forming and being transported past the advancing dendritic columnar front [1-3]. This may be a beneficial transition, as equiaxed grains are typically finer than columnar grains and may result in more isotropic mechanical properties. Thus, when a finer equiaxed structure is desired, it is common to introduce grain refiners within the melt that promote equiaxed growth [4, 5]. On the other hand, a CET occurring in a single crystal casting may result in non-uniformities in the microstructure and force the casting to be scrapped or repaired [6]. Free-floating dendrites may also be the source of significant macrosegregation [1,3], and grain refinement has been produced by fragmentation events in deeply undercooled melts [7]. Hence, a better understanding of the mechanisms of dendrite fragmentation is essential to control the microstructure selection during casting processes.

Fragmentation has been observed in transparent organic materials as early 1935 by Papapetrou [8], but visualizing the fragmentation of metallic dendrites has been made possible by the advancement of X-ray radiographic imaging [9-19]. Early X-ray radiography studies used to visualize dendrite fragmentation in metals were limited by a lack of spatial resolution and gray-level sensitivity [13]. However, these studies confirmed that, even though equiaxed grains can originate from nucleation events ahead of the columnar front and fragmentation events within the mushy zone [20], the latter has a predominant role in morphological transitions like CET.

Improvements in spatial resolution and gray-level sensitivity have now made it possible to observe higher density solute settling, enrichment of the liquid, and melting of dendrite roots during upward directional solidification experiments of an Al-20 wt% Cu alloy [16]. Hence, different growth directions yield significantly different microstructural outcomes, depending upon the respective solubility of the liquid and solid phases, their relative densities, and the orientation of the crystal growth and temperature gradient with respect to gravity [11,12,15,17]. The difference in alloy composition between Al-20 wt% Cu and Al-30 wt% Cu was also shown to have a significant effect on fragmentation rate [12], which was attributed to the greater buoyancy of fragmented dendrites in the more copper-rich liquid of the Al-30 wt% Cu alloy. Following a similar local solute enrichment mechanism, an increase of the interdendritic liquid flow with pulsed electromagnetic field has been shown to increase fragmentation rates [18,19]. Studies combining synchrotron X-ray radiography and topography have also brought evidence that fragmentation events are linked to mechanical strains in dendrite branches [21,22].

These combined studies have made it clear that a variety of effects may cause dendrite fragmentation, including curvature-driven solubility [23,24], latent heat release [25], mechanical constraints on dendritic sidebranches due to shear stress and gravity [21,22], and remelting of secondary dendrite arms, due to solute enrichment when gravity drives solute between primary dendritic trunks [16,26].

Yet, even though the critical role of fragmentation in the CET is now commonly accepted, the most likely conditions for fragmentation events are still not clearly understood. For instance, while a change in growth velocity seems to promote dendritic fragmentation events, perhaps promoted in a transient growth regime, it remains unclear whether fragmentation preferentially occurs during an increase [17] or a decrease [20] of growth velocity. Therefore, fragmentation mechanisms during dendritic solidification still warrant further investigation.

In the current paper, we highlight Sn-Bi alloy directional solidification experiments in the upward and downward directions and quantify fragmentation rate, as well as the location in space and time of these events with in-situ X-ray radiography. The choice of alloy and processing conditions may result in thin dendritic branches that are more likely to break off or remelt. With the rejection of heavier solute into the liquid, a significantly higher fragmentation rate is expected during upward solidification. However, even in our experiments with relatively low solid fractions, a higher fragmentation rate did not lead to microstructural transition, as the entrapment of dendritic fragments within the solid structure network prevented detached fragments from floating off into the liquid.

Methods

A Sn-39.5 wt% Bi alloy was cast and rolled to a thickness of 100 μm. For each experiment, a foil sample was held between two sheets of boron nitride, which were inserted into a furnace. The furnace is composed of two induction coils, located above and below the sample, and a steel rod that acts as a susceptor that is heated by the induction coils and transmits the heat to the sample. The ends of the susceptor rod are water-cooled, which makes it possible to achieve high heating and cooling rates.

In order to achieve directional solidification of the sample, we control the power delivered to the upper and lower induction coils to create a temperature gradient across the sample, and then decrease the temperature of both ends simultaneously to achieve a constant temperature gradient across the sample. Temperatures are controlled with thermocouples near the induction coils and are measured with independent thermocouples embedded in the susceptor rod, just outside the field of view. Additional details about the furnace can be found in [27].

We illustrate fragmentation mechanisms by focusing on two specific experiments corresponding to the processing parameters listed in Table 1. In one experiment (top-down), the solidification proceeds downward, i.e. parallel to gravity, and in the other (bottom-up) the solidification proceeds upward, i.e. anti-parallel to gravity. The corresponding velocities of the isotherms and steady state growth velocities are (top-down) 23 and (bottom-up) 21 μm/s. These velocities, as well as measured primary dendrite tip velocities discussed later in this article, are expressed in terms of the temperature gradient direction, rather than crystal orientation.

Experimental conditions	Temperature gradient (K/mm)	Cooling rate (K/min)	Isotherm speed (μm/s)	Average measured growth speed (μm/s)
Top-down	2.58	3.47	23	28
Bottom-up	-2.85	3.62	21	61

The experiments were performed at the Sector ID-32-C beamline of Argonne National Laboratory's Advanced Photon Source using a 28 keV beam. Conversion of the transmitted X-rays to visible light is done with a 30 μm thick scintillator at a distance of 300 mm from the sample. The visible light then passes through a magnifier and is recorded by a CCD camera with 1024 x 1280 pixels. This results in a pixel size of $(1.40\ \mu m)^2$ and an overall field of view of about 1.4 mm x 1.8 mm. Images were acquired using a 1 s exposure time and a frame rate of 0.85 Hz.

The raw images have artifacts due to the non-uniform intensity of the incoming X-ray beam. To account for this, the images were normalized by an average of several images of a fully liquid sample. Over the several minute duration of the experiments, the beam tends to shift by 5 to 10 micrometers. This shift is accounted and corrected for by aligning the baseline image to the remaining images using a parabolic-fit optimization scheme and mutual information as the metric for match quality [28].

The solidification front velocity was measured by tracking the individual dendrite tips over time using ImageJ [29], calculating the overall speed of each primary dendrite arm, and then averaging the individual dendrite velocities. Individual dendrite fragmentation events were manually measured and recorded, including the time and space coordinates of each event. For some alloys and conditions, using only two-dimensional projected X-ray images can be misleading [21,22]. In our experiments, since dendritic branches are thin and fragmentation events occur at low solid fraction, the buoyant motion of fragments is relatively easy to identify by looking for buoyant motion of detached fragments, such as the one illustrated in Figure 1.

Results

Image sequences for the top-down and bottom-up directional solidification experiments are shown in Figure 2. The locations of cumulative fragmentation events are circled. In addition to numerous fragmentation events, we observe bending of some dendritic branches. As noted by Reinhart, bending of primary dendritic trunks may occur without systematically leading to fragmentation [21,22]. We observe that the same phenomenon might happen to secondary sidebranches. For example, the sidebranch illustrated in Figure 3 bends, passing through a darker diffracting condition without breaking.

A first important observation that differentiates these two experimental conditions is the measured solidification front velocities. In the bottom-up experiment, the dendrites are growing at a speed of 61 μm/s, as compared to 28 μm/s in the top-down experiment. This difference is because the two observations occurred at different stages of transient growth, since the thermal conditions in both experiments result in similar isotherm velocities and therefore similar steady state growth velocities (see Table 1).

The second major difference between the experiments is the dendritic fragmentation rate (highlighted by the low density of red circles in Figures 2A-2C and high density in Figure 2D-2E). This behavior is linked the rejected solute in the liquid under the effect of gravity, which has already been observed and explained for lighter [12] or heavier [17] solid structures than the liquid. As illustrated in Figure 4, the higher density bismuth solute rejected into the liquid during solidification will sink within the liquid. In the case of bottom-up solidification (Figure 4B), the bismuth solute sinks between the primary branches of the solid structure, leading to density stratification and a stable system with respect to temperature and solute distribution [30]. The enrichment of solute between the primary branches is directly related to the remelting of secondary branch roots and high fragmentation rate [16]. In contrast, the solute in the top-down solidification experiment falls in advance of the growing dendrites, forming large solute plumes (Figure 4A).

These plumes disturb the stability of individual dendrite growth, making the growth behavior of the front less consistent over time. The evolution of individual dendrite tip growth velocities for the two experiments is shown in Figure 5. In the top-down experiment, some dendrites appear to stop temporarily before again accelerating to catch up with the solidification front.

The time and location of the fragmentation events were also measured. Figure 6 shows the resulting distributions of fragmentation events with distance from the solidification front and time spent in the mushy zone. Interestingly, while the magnitude of the fragmentation rate is significantly different (18 events for top-down solidification compared to 255 for the bottom-up case), the peaks of these distributions occur at a similar distance from the solidification front in both cases, near 1000 μm. This observation is a clear indication that the thermal conditions, which are nearly identical in both experiments, have a predominant effect on the location of the fragmentation events, rather than the solidification front growth velocity, which is significantly different in the two experiments.

The fact that most fragmentation events occur around 1000 μm from the solidification front also explains that no evidence of a CET was observed, despite numerous fragmentation events occurring in the bottom-up solidification experiments. Even though the solid fraction was low at the location of the fragmentation events, the detached fragments became trapped within the dendritic network, preventing them from floating away and growing as equiaxed dendrites in the liquid. As pointed out in [16], fragmentation events are more likely to trigger a CET if broken sidebranches can easily float away; thus, fragments are more likely to trigger CET if they occur close to a grain boundary [16]. They are also more likely to trigger CET if the growth direction of the primary dendrite arms is oriented with gravity, so that broken sidebranches can float straight upward to escape the dendritic array. Here, the high misorientation angle of the growth direction with respect to gravity (about 38˚) likely plays an additional role into retaining detached fragments within the solid structure.

Image intensity was processed to determine the time evolution of the solid fraction with a method proposed by Mirihanage and collaborators to quantitatively relate image intensity to local solid thickness [31]. The resulting volume fraction of solid, averaged over the field of view and plotted against time, appears in Figure 7. The time evolution plots of solid fraction are similar, which is consistent with the finding that even though the growth conditions in these two experiments are at different transient stages, the thermal conditions are similar.

This data was also used to determine the solid fraction as a function of distance behind the solidification front. The fragmentation rate as a function of local solid fraction is shown in Figure 8. As previously suggested, fragmentation events occur at low solid fractions. Here, the peak of the distribution is close to a volume fraction of 0.10. No fragmentation events occur at solid fractions higher than 0.15.

Conclusions

Dendrite arm fragmentation mechanisms in a Sn-39.5 wt% Bi alloy during directional solidification were observed in two experiments with the solidification direction parallel (top-down) or anti-parallel (bottom-up) to gravity. The solute distribution in the liquid was more stable during upward solidification, as expected, due to density stratification. The resulting solute enrichment between the primary dendrites resulted in a much higher fragmentation rate. In contrast, the top-down experiment resulted in an unstable solute configuration in the liquid, leading to plumes of highly concentrated liquid falling in advance of the solidification front. While the observations were made at different stages of transient growth, the highest fragmentation rates occurred at a similar distance from the solidification front, indicating the important influence of thermal conditions on the location of fragmentation events.

In the bottom-up experiment, despite the high fragmentation rate (over 250 fragmentation events identified), detached branch floatation and subsequent CET were not observed. This is because that detached fragments are trapped within the solid structure, due to both (i) the preferential location of fragmentation events further behind the growth front and (ii) the misorientation of the dendrites with respect to gravity. In this specific case, even though higher fragmentation rates occur at lower solid fractions, the fragments can not escape the solid dendritic network. While

fragmentation has a defining role in CET, these experiments illustrate that numerous additional criteria are important in triggering morphological transitions.

Acknowledgements

The authors would like to thank T.V. Beard, R.W. Hudson, B.S. Folks, D.A. Aragon, K.D. Clarke (LANL), and Alex Deriy (APS) for their support with experiment preparations. This research was supported by the U.S. Department of Energy, Office of Science, Basic Energy Sciences under AJC's Early Career Award. This research used resources of the Advanced Photon Source, a U.S. Department of Energy (DOE) Office of Science User Facility operated for the DOE Office of Science by Argonne National Laboratory under Contract No. DE-AC02-06CH11357 and Los Alamos National Laboratory, operated by Los Alamos National Security, LLC under contract DE-AC52-06NA25396 for the U.S. Department of Energy.

Figure Captions

Figure 1 – (A) A region with a dendrite arm fragmenting and floating away during bottom-up solidification and magnified images at (B) 50.7 s, (C) 51.9 s, and (D) 53.1 s.

Figure 2 – X-ray radiographs of top-down (top row) and bottom-up (bottom row) solidification. The images are at times of (A) 35 s, (B) 80 s, (C) 320 s, (D) 15 s, (E) 80 s, and (F) 320 s after the solidification front enters the field of view. The cumulative fragmentation events are highlighted with red circles. Several dendrites in (A) and (D) are labeled with numbers; these correspond to the labels in Figure 5. Movies of the full sequence of images are included in the supplemental materials.

Figure 3 – (A) A selected area showing the bending of a dendrite branch through a diffracting condition during bottom-up solidification and magnified images shown at (B) 5.9 s, (C) 9.4 s, (D) 48.4 s.

Figure 4 – Normalized radiographs showing the distribution of solute for (A) top-down and (B) bottom-up solidification. Both images are normalized by a fully liquid image; therefore, a value less than one indicates solute enrichment and a value greater than one indicates solute depletion. Note the plumes that form during top-down solidification compared to the stable solute configuration that forms during bottom-up solidification. Movies showing the entire solidification sequence are included in the supplemental materials.

Figure 5 – Dendrite tip speeds for (A) top-down and (B) bottom-up solidification. Note how some dendrite tip speeds drop to almost zero during top-down solidification, due to the solute plumes affecting the supersaturation in front of the dendrites. The labels correspond to dendrites labeled in Figure 2.

Figure 6 – Fragmentation rates for (A) top-down and (B) bottom-up solidification. The distributions are plotted as both a histogram and a Gaussian kernel density estimation.

Figure 7 – Time evolution of the volume fractions of solid for the two experiments.

Figure 8 – Dendrite fragmentation rate as a function of solid fraction for (A) top-down and (B) bottom-up solidification with both a histogram and a Gaussian kernel density estimation.

References

1. M.C. Flemings. *Solidification Processing*, McGraw-Hill, January 1974.
2. A. Hellawell, S. Liu, S.Z. Lu, *JOM* 49, 18 (1997).
3. C. J. Vreeman, M.J.M. Krane, and F.P. Incropera, *Int. J. Heat Mass Trans.* 43, 677 (2000).
4. A.L. Greer, P.S. Cooper, M.W. Meredith, W. Schneider, P. Schumacher, J.A. Spittle, A. Tronche, *Adv. Eng. Mater.* 5, 81 (2003).
5. T.E. Quested, *Mater. Sci. Tech.* 20, 1357 (2004).
6. A. de Bussac, and Ch.-A. Gandin, *Mat. Sci. Eng. A* 237, 35 (1997).
7. D.M. Herlach, K. Eckler, A. Karma, M. Schwarz, *Mat. Sci. Eng. A* 304–306 20 (2001).
8. A. Papapetrou, *Z. Krist*. 92, 2 (1935)
9. R.H. Mathiesen, L. Arnberg, F. Mo, T. Weitkamp, and A. Snigirev, *Phys. Rev. Lett.* 83, 5062 (1999)
10. R.H. Mathiesen, L. Arnberg, K. Ramsøskar, T. Weitkamp, C. Rau, and A. Snigirev, *Met. Mat. Trans. B* 33, 613 (2002)
11. R.H. Mathiesen, and L. Arnberg, *Acta Mat.* 53, 947 (2005)
12. R.H. Mathiesen, L. Arnberg, P. Bleuet, and A. Somogyi, *Met. Mater. Trans. A* 37 2515 (2006)
13. H. Yasuda, I. Ohnaka, K. Kawasaki, A. Sugiyama, T. Ohmichi, J. Iwane, and K. Umetani, *J. Cryst. Growth* 262, 645 (2004)
14. G. Reinhart, N. Mangelinck-Noel, H. Nguyen-Thi, T. Schenk, J. Gastaldi, B. Billia, P. Pino, J. Hartwig, J. Baruchel, *Mat. Sci. Eng. A* 413, 384 (2005)
15. L. Arnberg, and R.H. Mathiesen, *JOM* 59, 1543 (2007)
16. D. Ruvalcaba, R.H. Mathiesen, D.G. Eskin, L. Arnberg and L. Katgerman, *Acta Mat.* 55, 4287 (2007)
17. S. Boden, B. Willers, S. Eckert, and G. Gerbeth, *Int. J. Cast. Metals Res.*22, 30 (2009)
18. E. Liotti, A. Lui, R. Vincent, S. Kumar, Z.P. Guo, T. Connolley, M. Hart, L. Arnberg, R.H. Mathiesen, and P.S. Grant, *Mat. Sci. Forum* 765, 210 (2013)
19. E. Liotti, A. Lui, R. Vincent, S. Kumar, Z. Guo, T. Connolley, I.P. Dolbnya, M. Hart, L. Arnberg, R.H. Mathiesen, and P.S. Grant, *Acta Mat.* 70, 228 (2014)
20. H. Yasuda, Y. Yamamoto, N. Nakatsuka, M. Yoshiya, T. Nagira, A. Sugiyama, I. Ohnaka, K. Uesugi, and K. Umetani. *Int. J. Cast Metals Res.* 22, no. 1-4 (2009): 15-21.
21. G. Reinhart, A. Buffet, H. Nguyen-Thi, B. Billia, H. Jung, N. Mangelinck-Noel, N. Bergeon, T. Schenk, J. Härtwig, J. Baruchel, *Met. Mater. Tran. A* 39, 865 (2008).
22. G. Reinhart, H. Nguyen-Thi, N. Mangelinck-Noël, J. Baruchel, B. Billia, *JOM*, 66, 1408 (2014)
23. T.Z. Kattamis, J.C. Coughlin, and M.C. Flemings, *AIME Met. Soc. Trans.* 239, 1504
24. M. Kahlweit, *Scripta Met.* 2, 251 (1968)
25. M. Schwarz, A. Karma, K. Eckler and D.M. Herlach, *Phys. Rev. Lett.* 73, 1380 (1994)

26. A. Kumar, and P. Dutta, *J. Phys. D Appl. Phys.* 41, 15501 (2008)
27. A.J. Clarke, D. Tourret, S.D. Imhoff, P.J. Gibbs, K. Fezzaa, J.C. Cooley, W.-K. Lee, A. Deriy, B.M. Patterson, P.A. Papin, K.D. Clarke, R.D. Field, J.L. Smith, *Adv. Eng. Mat.* 17, 454 (2015)
28. E.B Gulsoy, J.P. Simmons, M, De Graef, *Scripta Mater.* 60, 381 (2009).
29. Rasband, W.S., ImageJ, U. S. National Institutes of Health, Bethesda, Maryland, USA, http://imagej.nih.gov/ij/, 1997-2014.
30. S.R. Coriell, M.R. Cordes, W.J. Boettinger, R.F. Sekerka, *J. Cryst. Growth* 49, 13 (1980).
31. W.U. Mirihanage, K.V. Falch, I. Snigireva, A. Snigirev, Y.J. Li, L. Arnberg, R.H. Mathiesen, *Acta Mater.* 81, 241 (2014).

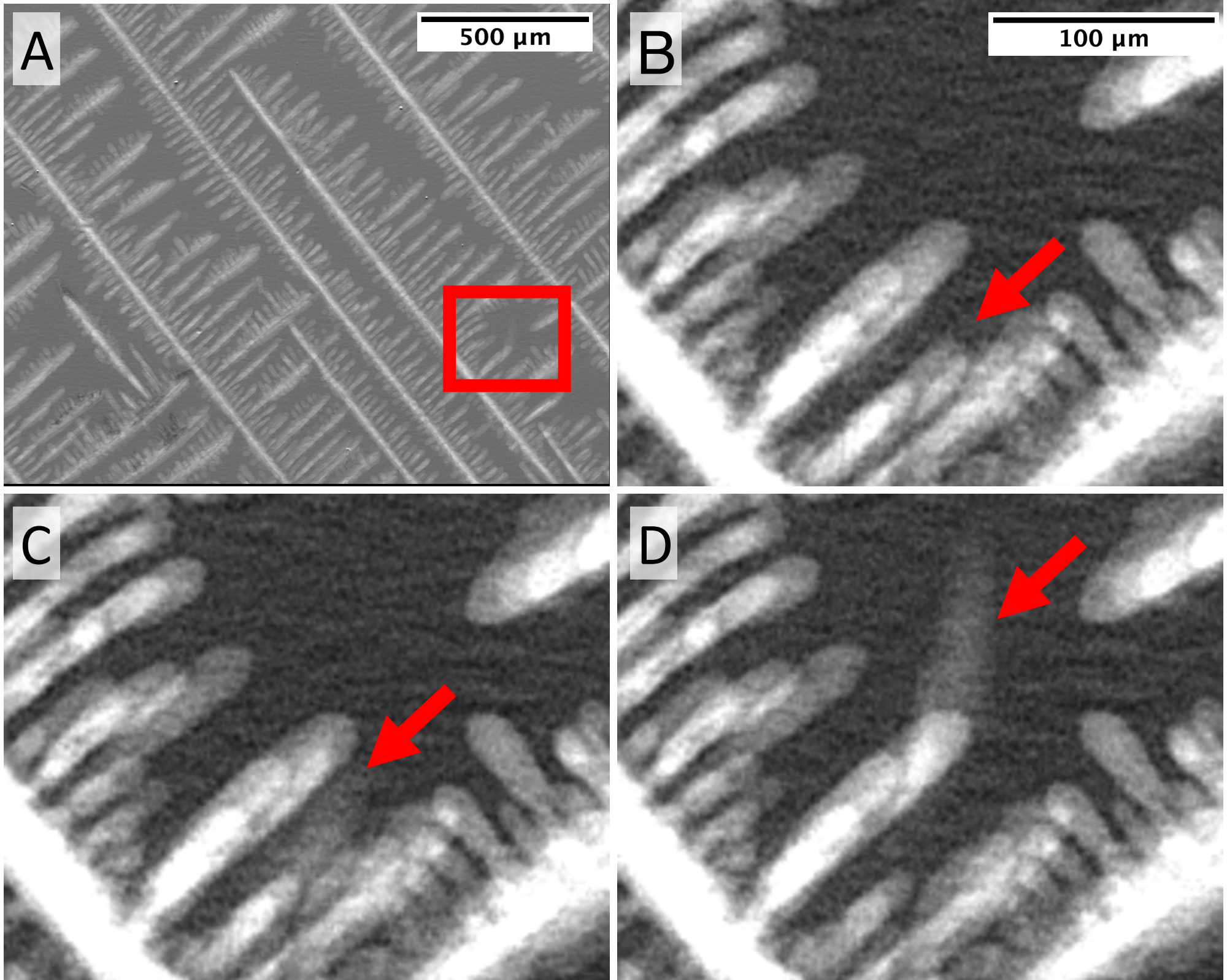
A
500 µm
B
100 µm
C
D

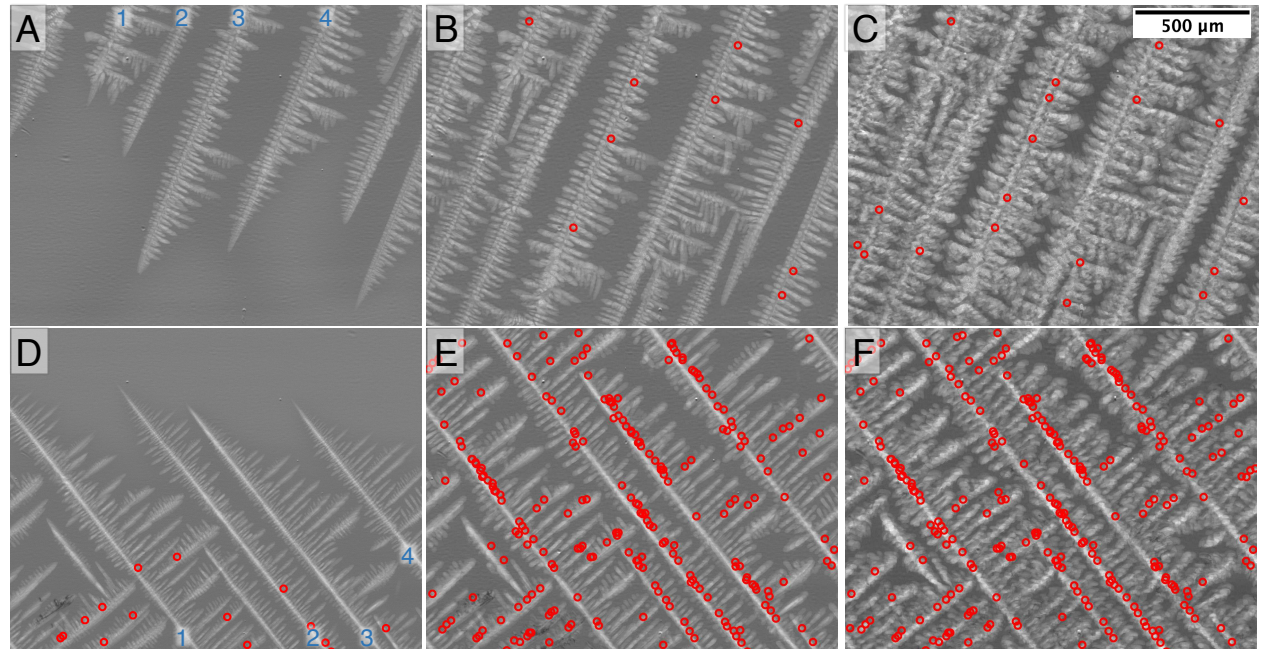
A
1
2
3
4
B
C
500 µm
D
1
2
3
4
E
F

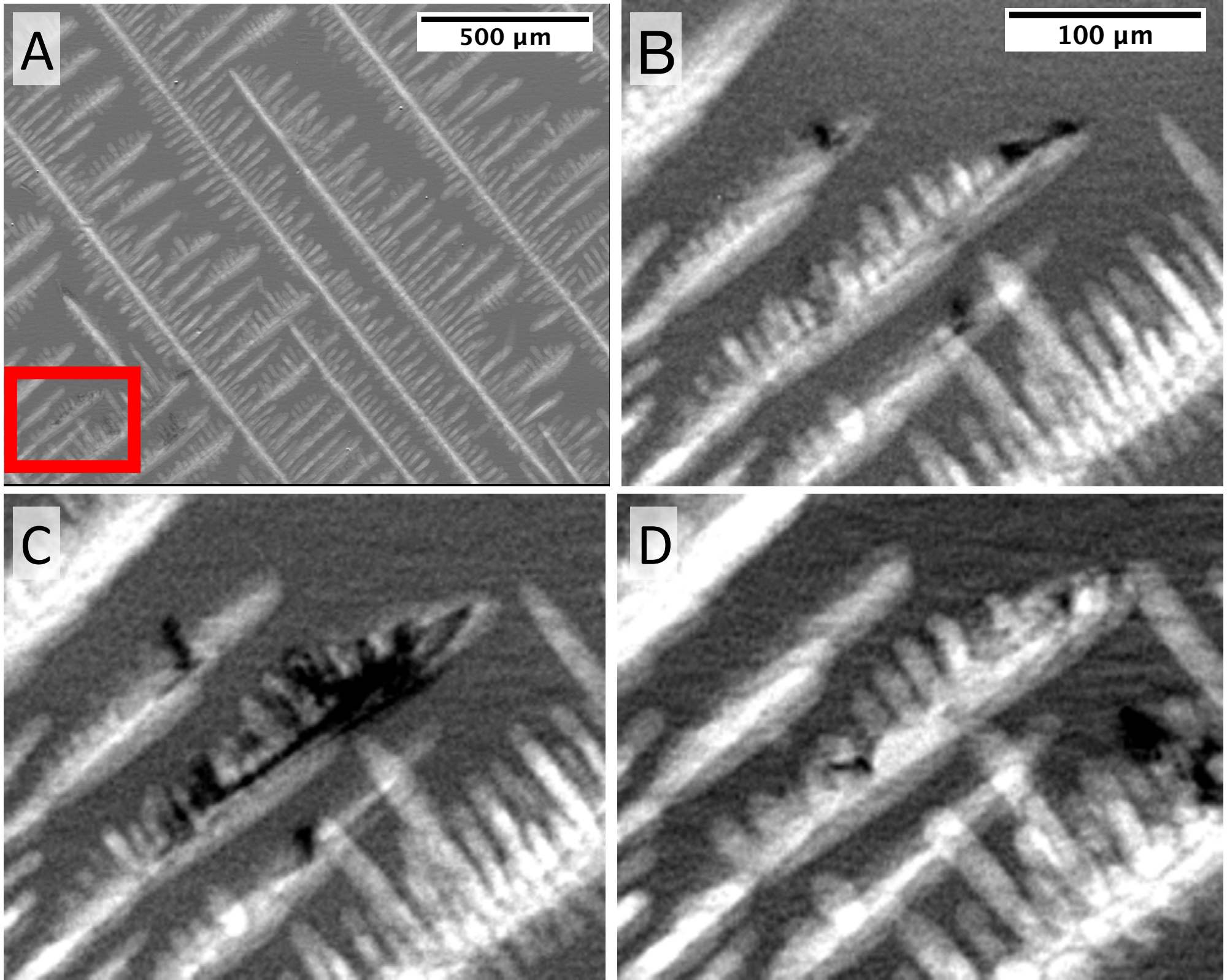
A
500 µm
B
100 µm
C
D

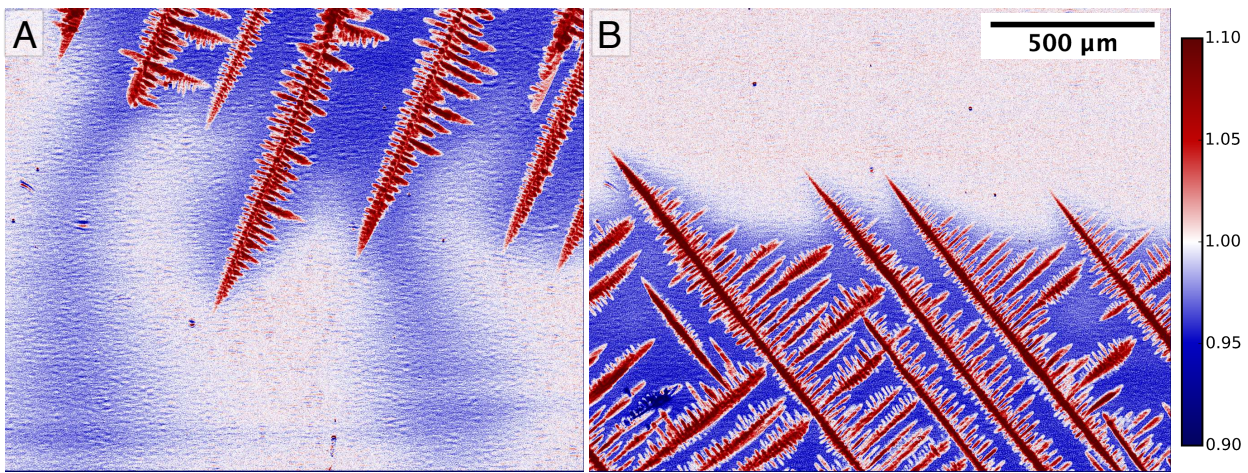
A
B
500 µm
1.10
1.05
1.00
0.95
0.90

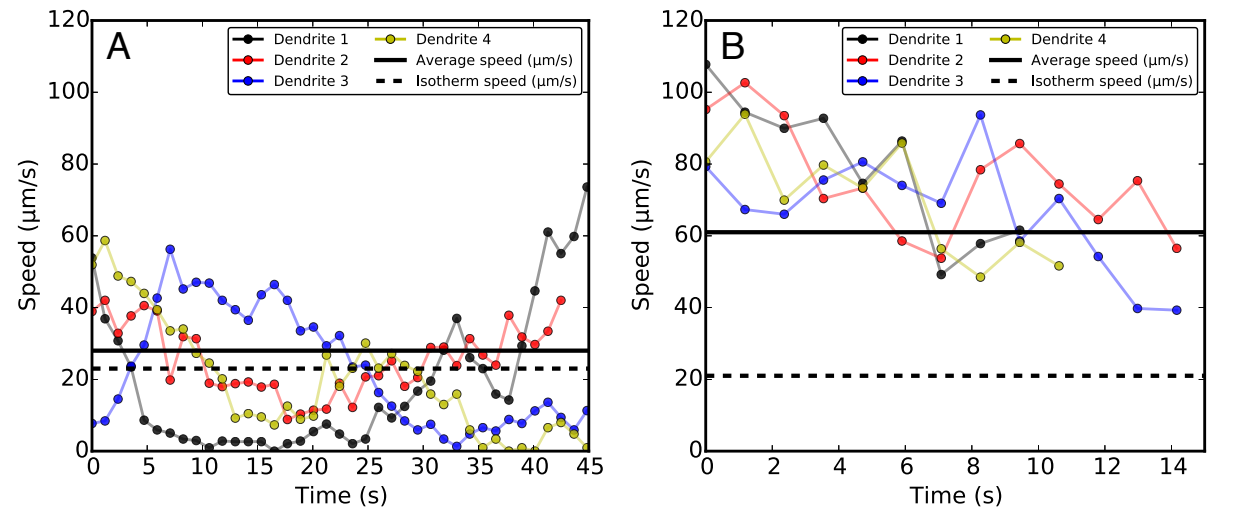
A
B
Dendrite 1
Dendrite 2
Dendrite 3
Dendrite 4
Average speed (μm/s)
Isotherm speed (μm/s)
Speed (μm/s)
Time (s)

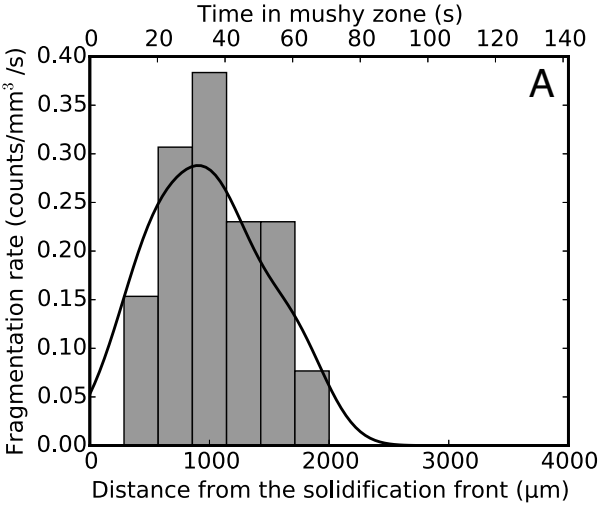
Time in mushy zone (s)
0
20
40
60
80
100
120
140
A
Fragmentation rate (counts/mm^3/s)
0.00
0.05
0.10
0.15
0.20
0.25
0.30
0.35
0.40
0
1000
2000
3000
4000
Distance from the solidification front (μm)

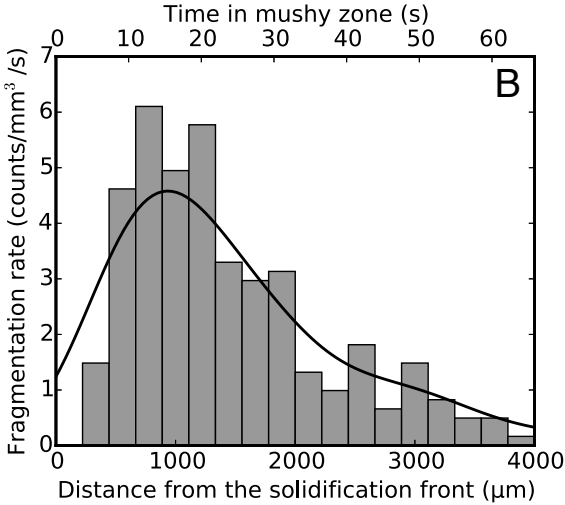
Time in mushy zone (s)
0
10
20
30
40
50
60
B
Fragmentation rate (counts/mm^3/s)
0
1
2
3
4
5
6
7
0
1000
2000
3000
4000
Distance from the solidification front (μm)

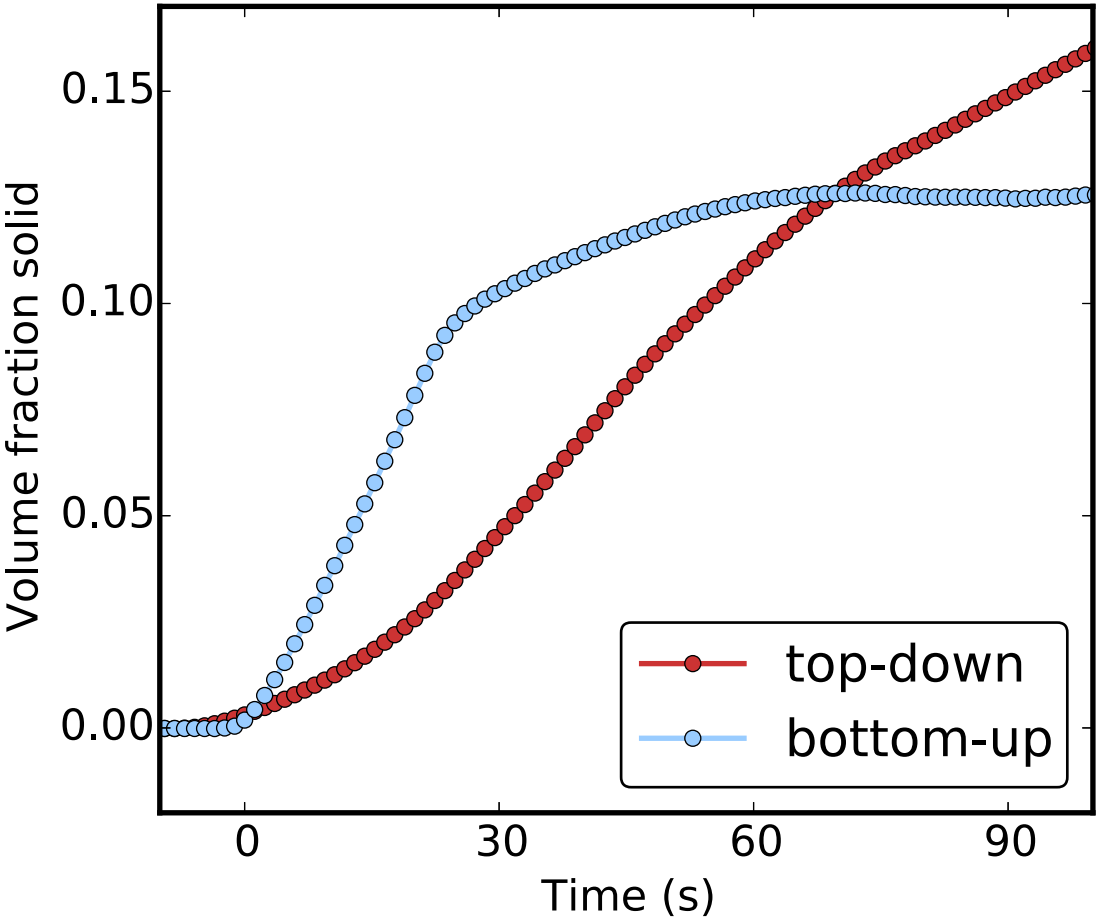
0.15
0.10
0.05
0.00
Volume fraction solid
0
30
60
90
Time (s)
top-down
bottom-up

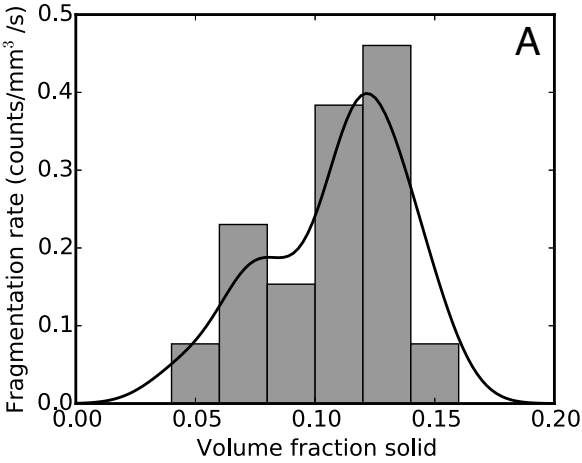
A
Fragmentation rate (counts/mm^3/s)
0.0
0.1
0.2
0.3
0.4
0.5
0.00
0.05
0.10
0.15
0.20
Volume fraction solid

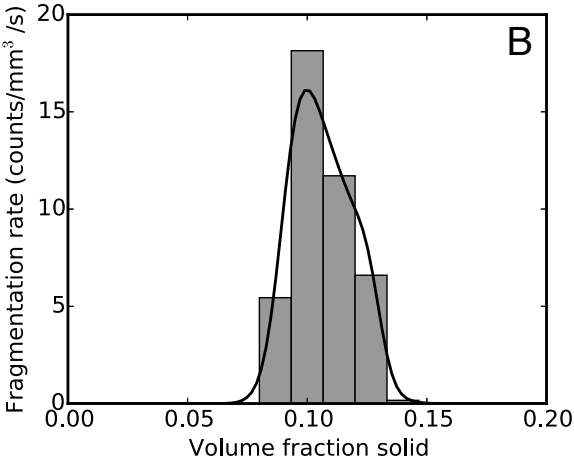
B
Fragmentation rate (counts/mm^3/s)
0
5
10
15
20
0.00
0.05
0.10
0.15
0.20
Volume fraction solid